Petroleum Science 23 (2026) 2758–2772

Contents lists available at ScienceDirect

Petroleum Science

journal homepage: www.keaipublishing.com/en/journals/petroleum-science

Original Paper

# Embedment behavior of variable-radius indenters in shale: A combined experimental and theoretical approach

Yong-Xin Che [a], Ling-Zhi Xie [a,b,*], Bo He [a], Yu-Xuan Liu [c], Feng-Xia Li [d], Yao Zhang [b]

[a] Institute of New Energy and Low-Carbon Technology, Sichuan University, Chengdu, 610207, Sichuan, China
[b] State Key Laboratory of Hydraulic and Mountain River Engineering, College of Architecture and Environment, Sichuan University, Chengdu, 610065, Sichuan, China
[c] State Key Laboratory of Oil and Gas Reservoir Geology and Exploitation, Southwest Petroleum University, Chengdu, 610500, Sichuan, China
[d] SINOPEC Petroleum Exploration and Production Research Institute, Beijing, 100083, China

ARTICLE INFO

*Article history:*
Received 20 August 2025
Received in revised form
4 November 2025
Accepted 7 April 2026
Available online 9 April 2026

Edited by Xiu-Fang Hu

*Keywords:*
Shale
Proppant embedment
Radius effect
Elastoplastic properties
Embedment depth modeling

ABSTRACT

During the shale gas extraction, a larger fracture closure stress causes proppants to embed in the shale surface, greatly reducing fracture conductivity. The heterogeneity of shale makes its mechanical properties exhibit obvious scale effects, and the embedment behavior of proppants of different sizes is thus affected by multi-scale mechanical responses. To investigate the effect of particle size on the embedment mechanism, this work conducted micro-indentation tests using indenters of varying radii to model the embedment process of a single proppant. The test results show that when the embedment depth is 1 μm, with the radius increasing from 25 μm to 400 μm, the corresponding load does not show a linear growth trend, while the Young's modulus increases by about 76%. When the embedment depth is 3 μm, 5 μm, and 10 μm, respectively, the load gradually increases with the increase in radius. It is worth noting that when the embedment depth reaches 10 μm, the Young's modulus corresponding to each particle size tends to be stable, about 25 GPa. Based on the Drucker-Prager yield criterion, an analysis model of proppant embedment depth considering the particle size effect was established. Compared with the traditional Hertz and Thornton models, the proposed model can more accurately reflect the plastic behavior and strengthening mechanism of shale, and is applicable for predicting and evaluating multi-scale embedment responses.


## 1. Introduction

As an important unconventional oil and gas resource, shale gas plays an extremely significant role in optimizing global energy structure and achieving clean and low-carbon development (Chen et al., 2022; Katende et al., 2023a; Liu et al., 2025a; Middleton et al., 2017). Hydraulic fracturing technology is commonly utilized in the extraction of shale gas to create a network of conductive fractures with high-pressure fluid injection, which increases reservoir permeability and productivity (Liu et al., 2025b; Zhang et al., 2024). The proppant is used to hold the fractures open after the drilling fluid flows back into the wellbore (Katende et al., 2023b; Liu et al., 2025c; Wu et al., 2025). However, the higher plasticity and in-situ stresses of the deep shale reservoir make proppants extremely prone to embed into the fracture surface (Ahamed et al., 2019; Fan et al., 2019; Zhi and Elsworth, 2020). Research has shown that the proppant embedment can decrease fracture width by 10%–60%, and a 20% drop in fracture width can result in a 50%–60% decrease in fracture conductivity (Arshadi et al., 2017). Thus, it is necessary to understand the proppant embedment behavior to determine the evolution law of fracture conductivity in deep shale reservoirs.

The proppant size range lies between 4 mesh and 400 mesh (sieve aperture between 4.75 mm and 0.038 mm) (Liang et al., 2016). Proppants of various sizes were generally mixed in hybrid completion designs to improve fracture conductivity (Liu et al., 2021a, 2024; Shaibu et al., 2022). Research has indicated that augmenting the percentage of large-size proppants can

* Corresponding author.
*E-mail address:* xielingzhi@scu.edu.cn (L.-Z. Xie).
Peer review under the responsibility of China University of Petroleum (Beijing).

https://doi.org/10.1016/j.petsci.2026.04.007

considerably improve the conductivity because of the large-size proppant pack's high porosity and resistance to high closure stress (Bandara et al., 2021; Fan et al., 2020) Proppants with smaller sizes have the potential to decrease permeability in stimulation treatments (Katende et al., 2023b). The force carried by each proppant is smaller, which results in less embedment at a given stress level (Bandara et al., 2021). The above research on multi-size proppants is primarily on the macro-mixed embedment, which is a comprehensive response of multiple particles. The macroscopic multi-particle research is still faced with the difficulty of theoretical model construction, and the formed models are empirical (Katende et al., 2021a). Compared to single-particle embedment, there are complex interactions between multiple particles, such as friction and extrusion pressure (Li et al., 2022). He (2021) used discrete element method (DEM) to simulate the embedment behavior of multi-particle proppants and investigated the impact of stress interference between adjacent proppants on the embedment depth. The embedment depth of the multi-particle proppant increases by no more than 15% compared to the embedment depth of the single particle due to the stress interference, and the embedment depth growth rate quickly decreases as the particle distance increases. Therefore, the complex multi-particle proppant embedment behavior can be approximated by the contact between a single particle and an infinite plate when the impact of particle interference on the embedment is ignored. Fig. 1 shows a schematic study of the mechanism from multi-size proppant packing to a single particle.

The proppant embedment behavior in shale can be abstracted as the interaction between a rigid spherical indenter and a semi-infinite medium (Guo et al., 2017; Katende et al., 2021b). The classic Hertz contact model can describe this embedment process (Hertz, 1882). Thornton (1997) treated the contact body as an elastic-perfectly plastic material, obtaining an elastoplastic embedment model for a spherical indenter. Because of the high temperature and high in-situ stress conditions seen in deep reservoirs, shale displays elastoplastic mechanical characteristics (Rybacki et al., 2016). The Hertz model underestimated the embedment depth (Chen et al., 2018), while the elastic-perfectly plastic model overestimated the embedment depth (Ghaednia et al., 2020). To make the embedment depth model more closely align with test results (load-displacement curve), many studies have used linear strengthening (Wang et al., 2020) and nonlinear strengthening laws (Big-Alabo et al., 2015; Larsson and Olsson, 2016; Olsson and Larsson, 2016; Zhao et al., 2015) to explain the mechanical behavior of the contact body during the plastic yield phase, obtaining an elastoplastic strengthening model that lies between the Hertz and the Thornton model. Wang et al. (2020) discussed the influence of the macroscopic strengthening coefficient on the curve of a linear embedment model. However, the related models are mostly based on macroscopic mechanical parameters, which make it difficult to accurately reflect the local elastoplastic deformation characteristics of proppant embedded in shale. After the proppant is embedment into the shale, the shale does not overall fracture but only experiences local plastic deformation at the embedment location. As a result, the strengthening model based on macro-mechanical parameters cannot accurately describe the elastoplastic embedment behavior at the proppant scale.

The Hertz contact theory has pointed out that the embedment depth is closely related to the indenter radius, but the theory is based on the ideal elastic body assumption, which is difficult to cover the heterogeneity and plastic characteristics of shale materials (Das et al., 2021; Deng et al., 2024; Ulm et al., 2007). The contact area of the proppants with different particle sizes in shale is different, and the embedment depth and load response are easily affected by the multi-scale mechanical properties of shale. Current studies on proppant embedment concentrate on spherical indentation with a single particle size (Alagoz et al., 2021; Zheng et al., 2019). There is still a lack of systematic research on the embedment mechanism of proppants with different particle sizes, especially since the mechanical modeling under the dominant condition of elastic-plastic response is still not perfect.

For this purpose, this paper carried out micro-indentation tests with different radius indenter (25 μm, 100 μm, 200 μm, and 400 μm) to simulate the embedment behavior of proppant in shale. The relationships between particle size, embedment depth, and mechanical response were systematically analyzed. Based on the Drucker-Prager yield criterion and the elastic-plastic characteristics of shale, a prediction model of proppant embedment depth considering particle size effect is further established, which aims to provide a theoretical basis for proppant selection and fracture conductivity evaluation in shale reservoirs.

## 2. Experimental methods

### 2.1. Sample collection and preparation

Fig. 2 shows the complete test process from sample and indenter preparation to the conduct of the indentation test. Fig. 2(a) shows a

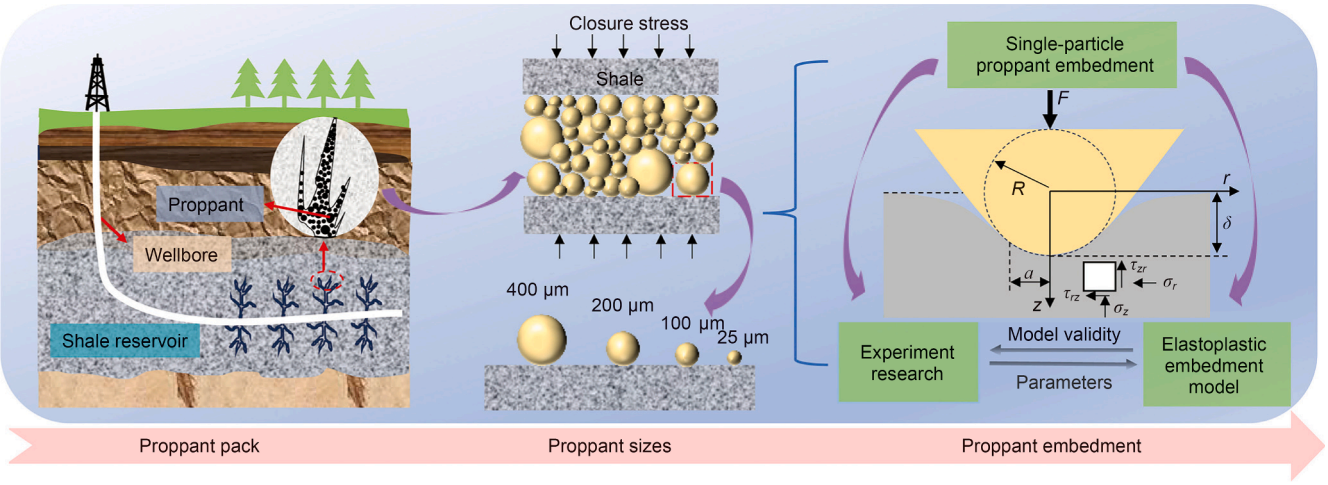


**Fig. 1.** Schematic diagram of multi-particle proppant packing to a single-particle embedment.

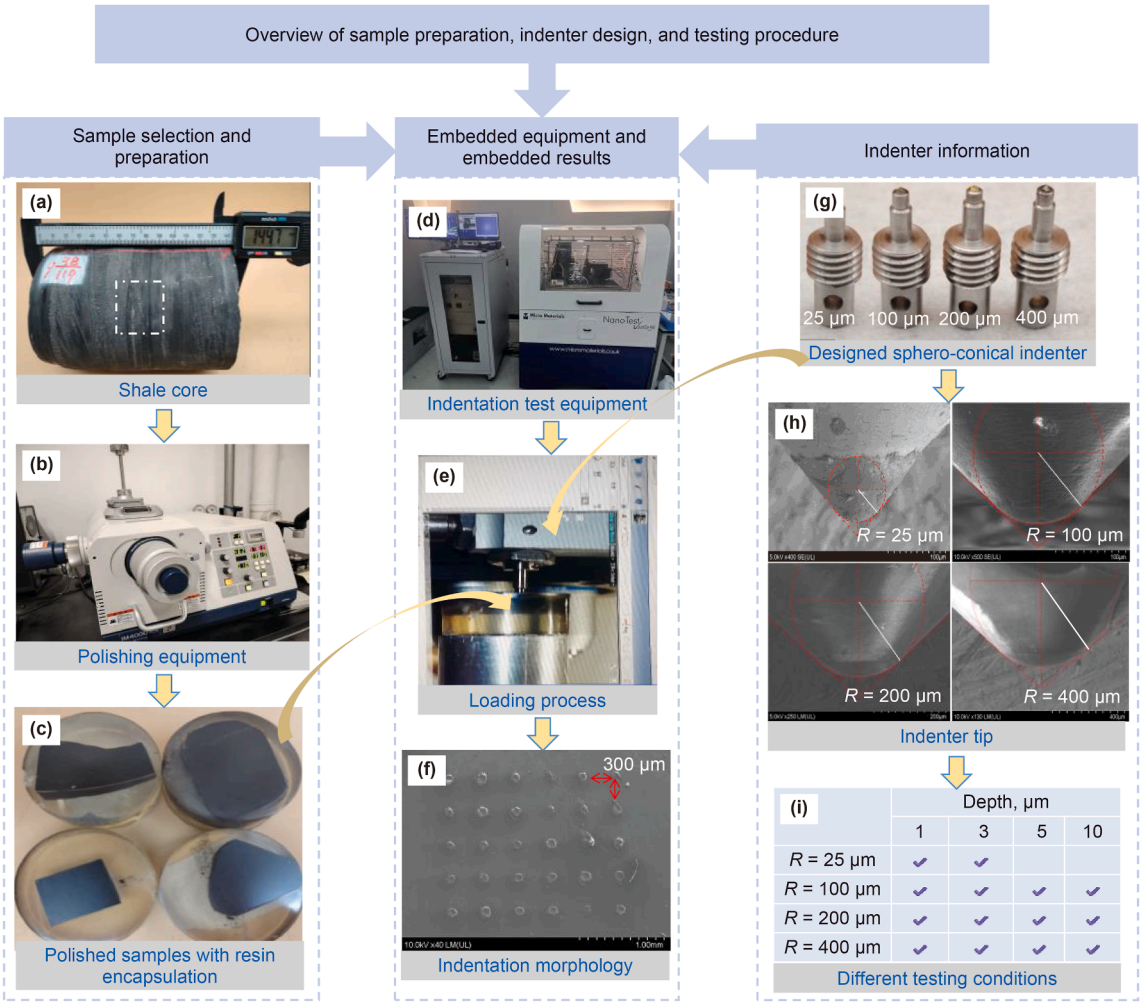


**Fig. 2.** Embedment test process. **(a)** The Longmaxi shale core, **(b)** polishing equipment, **(c)** polished samples with resin encapsulation, **(d)** indentation test equipment, **(e)** loading process, **(f)** indentation morphology, **(g)** indenters, **(h)** indenter tip, **(i)** different testing conditions.

shale core sample from the Silurian Longmaxi Formation in PY well, southeastern Chongqing, China, at a depth of 2100 m. The mechanical characteristics of shale are related to the basic composition information of clay, hard minerals, and organic matter. Table 1 shows the X-ray diffraction (XRD) analysis results. The total organic carbon (TOC) content of the core sample is 3.56 wt%.

First, the 3 cm × 3 cm × 3 cm cube area with a uniform texture and no flaws is chosen from a rock core, as seen in Fig. 2(a). Then, specimens of different sizes were cut from this 3 cm × 3 cm × 3 cm area for indentation testing. Generally, polishing treatment is required on the samples before indentation testing to reduce the impact of surface roughness on the test results. Various silicon carbide abrasive papers ranging from 200 to 10,000 grit were used to polish the sample surface. Subsequently, an IM4000 argon ion mill operated at 4.0 kV, and a 5° angle was used for polishing for 2 h to achieve a completely flat surface, as shown in Fig. 2(b). The samples are stored at room temperature. The polished sample in Fig. 2(c) is coated with resin to ensure that it can easily be fixed to the loading platform.

### 2.2. Design of a sphero-conical indenter

The term 'sieve cut' refers to the proppant when detailing the proppant size, e.g., 20/40 mesh is labeled 850 μm and 425 μm; 40/70 mesh is 425 μm and 212 μm; and 70/140 mesh is 212 μm and 106 μm. Currently, proppants of 20/40, 30/50, 40/70, and 70/140 mesh are widely used in hydraulic fracturing (Zhang et al., 2021). Because the roundness and sphericity of the proppant can reach 0.9 (Katende et al., 2021a), the proppant is regarded as an ideal spherical particle. The hardness of commonly used proppants, such as quartz sand and ceramics, typically ranges from 8 GPa to 12 GPa, which is significantly lower than that of diamond (80–100 GPa). During the interaction between real proppants and shale, the measured displacement includes not only the embedment depth but also the deformation of the proppant itself. These two effects are extremely difficult to separate in microscopic testing. To isolate and clarify the contribution of embedment behavior, this study employs diamond material as a surrogate for proppants. Owing to its extremely high hardness and elastic

**Table 1**
The XRD analysis results showing the mass fraction of different mineral phases in the studied core sample.

| Quartz | Clay minerals | Calcite | Sodium feldspar | Dolomite | Potassium feldspar | Pyrite |
|---|---|---|---|---|---|---|
| 37% | 34.2% | 7.7% | 10.9% | 5.1% | 3.2% | 1.9% |

modulus, the diamond tip ensures negligible deformation during penetration, thereby eliminating the influence of proppant deformation on embedment measurements.

Accordingly, four types of sphero-conical indenters were designed as shown in Fig. 2(g) with radii of 25 μm (about 270 mesh), 100 μm (about 70 mesh), 200 μm (about 40 mesh), and 400 μm (about 20 mesh), respectively. Each indenter consisted of two parts: a diamond tip and a high-strength steel base. The diamond tip provided excellent hardness and wear resistance, while the steel base ensured mechanical stability during loading. Fig. 2(h) shows the tip of sphero-conical indenters with different radii. The indenter tips were composed of diamond materials, having a Young's modulus of 1140 GPa and a Poisson's ratio of 0.07. In this experiment, the radius of curvature of the conical indenter is regarded as the radius $R$ of the spherical particle.

The maximum embedment depth is related to the height of the indenter spherical cap. According to the indentation test procedure, the maximum indentation depth cannot exceed half of the spherical cap height. For the 25 μm radius indenter, this maximum allowable depth is approximately 3 μm. To ensure reliable and accurate results, we only adopted the embedment depth ($D$) for this radius to 1 μm and 3 μm. A total of 14 testing conditions were carried out under different radii ($R$) by the four kinds of indenters, as shown in Fig. 2(i). For each testing condition, points of about 30 indents were tested in a 5 × 6 network. The total number of indentation test points is 420.

### 2.3. Micro-indentation test

The micro-indentation testing with the four types of sphero-conical indenters is conducted by the micro-indentation module of the NanoTest Vantage system (Micro Materials Ltd., UK), which is shown in Fig. 2(d). Prior to testing, the indentation system was calibrated using a standard fused silica reference sample to correct for load-displacement compliance and to guarantee measurement reliability. The equipment allows precise control of loading and displacement during micro-indentation testing. The system has a load resolution of 50 nN and a displacement resolution of 0.005 nm, with a data acquisition frequency of 100 Hz during the indentation process, ensuring accurate capture of the loading–unloading curve. All indentation tests were conducted under laboratory conditions at a temperature of approximately 25 ± 2 °C and a relative humidity of 50% ± 5%. The displacement-control mode was adopted for the loading/unloading. The quasi-static constant loading mode was applied at a loading/unloading rate of 0.1 μm/s. This test only includes loading and unloading and does not have a load-holding stage. The micro-indentation was carried out using indenters with radii of 25 μm, 100 μm, 200 μm, and 400 μm, respectively. The maximum target embedment depth is set as 1 μm, 3 μm, 5 μm, and 10 μm, respectively. According to the test requirements, the indentation shall be spaced at approximately three to five times its diameter (Fischer-Cripps, 2011). Therefore, the spacing between adjacent points of different radii was 75 μm, 300 μm, 600 μm, and 1200 μm, respectively. The loading process is shown in Fig. 2(e). The load-displacement curve was experimentally obtained, which could be distinctly divided into the loading segment and the unloading segment, reflecting the material's elastic-plastic response. When the indenter is unloaded, the elastic deformation of the sample surface recovers, while the plastic deformation remains unchanged, resulting in residual deformation. Fig. 2(f) shows the residual indentation on the sample surface obtained through scanning electron microscopy (SEM). All SEM images in the text were obtained in the secondary electron (SE) mode.

The unloading segment is analyzed by Oliver and Pharr (1992) to obtain the contact stiffness $S$, from which the elastic modulus $E$ are calculated:

$$E = \frac{\sqrt{\pi}}{2}\frac{S}{\sqrt{A_c}} \tag{1}$$

where $S = \mathrm{d}P/\mathrm{d}h$ is the initial slope of the unloading segment, and $A_c$ is the projected area of the contact, $A_c \approx 2\pi R h_c$ (Fischer-Cripps, 2011). The contact depth $h_c$ was determined from the unloading stiffness and maximum load using their formulation, $h_c = h_{max} - h_s$. The displacement of the surface at the perimeter of the contact is $h_s$, $h_s = \varepsilon\frac{P_{max}}{S}$. For spherical indenters, $\varepsilon = 0.75$ (Oliver and Pharr, 1992). $P_{max}$ is the maximum indentation load. $h_{max}$ is the maximum depth.

## 3. Experimental results

### 3.1. Load-displacement curve evolution

The load-displacement curve represents the mechanical response of the shale–indenter interaction, and it may be used to intuitively determine the behavior differences between different indenters in the embedmntment process (Fischer-Cripps, 2007; Murthy, 2021). Fig. 3 displays the load-displacement curve for various radius indenters at different desired embedment depth. It shows that there is no "pop-in" phenomenon and that the loading curves of various radii are generally smooth; there is significant dispersion in load-displacement curves during testing, such that the same embedment depth often corresponds to different loads; and the required load for indenters with different radii gradually increases as the embedment depth increases. The observed variations in indentation responses at different positions, under the same indenter radius and loading conditions, are primarily attributed to the heterogeneity of shale, which manifests in mineralogical composition and microstructural differences. Note that there is a discrepancy in embedment depth between the targeted and the actual because of the influence of the material itself. This phenomenon was also observed by Bennett (2016).

The average curve provides a statistical description of the mechanical response for specific experimental conditions (Liu et al., 2022b). To illustrate the general trend, load-displacement curves were resampled using linear interpolation at a fixed displacement interval of 50 nm, aligned on the displacement axis, and then averaged point by point. The 30 blue curves in the figure are the experimental indentation curves, while the red curve is the average curve. It can be seen from Fig. 3 that the indentation curves of different points are close to the average curve in morphology and value. These averaged curves provide a more reliable basis for comparing the indentation behavior under different embedment depths and indenter radii.

### 3.2. Variation in average load

To account for the material heterogeneity and the limited number of indents, the averaged load values at each embedment depth were statistically processed and plotted as grouped bar charts with 95% confidence intervals, as shown in Fig. 4. The error bars illustrate the degree of variability at each condition, ensuring that the comparisons among different indenter sizes are statistically meaningful. The figure reveals that the average load gradually increases as the indenter radii increase at the same embedment depth. When the embedment depth is 1 μm, the change in average load with increasing indenter radius is not significant. The average

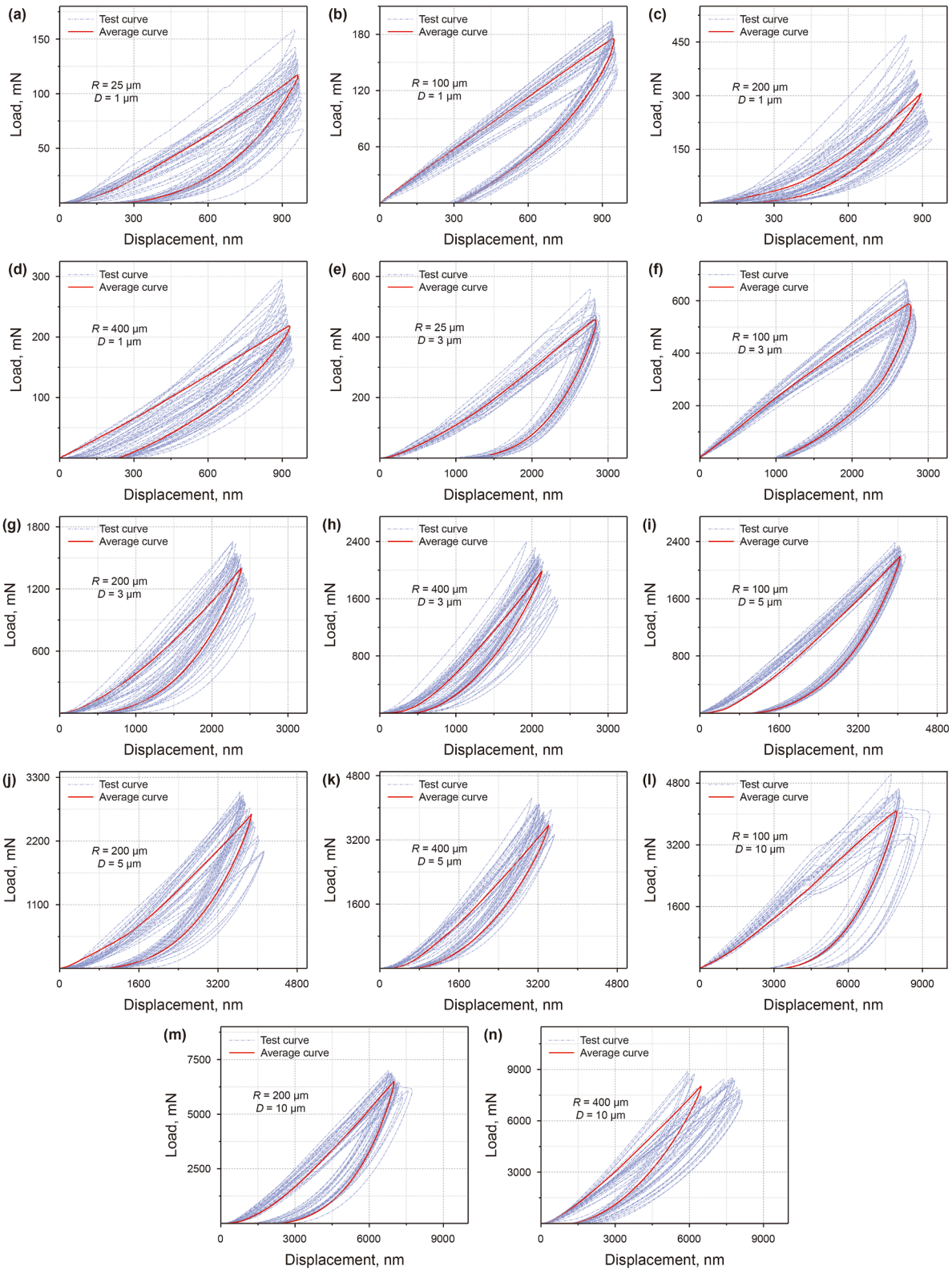


**Fig. 3.** Load-displacement curves (blue) and average curves (red) at different embedment depth ($D$) with different radii ($R$).

load steadily rises as the indenter radius grows at deeper embedment depths. The variation trend of load shows that, when the embedment depth is low, the embedment behavior is less affected by the indenter radius. The effect of the indenter radii on the embedment gradually becomes apparent with the increase in embedment depth. For a 25-μm radius, the load increases from 114.1 ± 19.32 mN at 1 μm depth to 451.91 ± 49.24 mN at 3 μm depth, showing moderate growth and relatively large variability, which may be related to surface roughness and local heterogeneity. For a 100-μm radius, the load rises steadily from

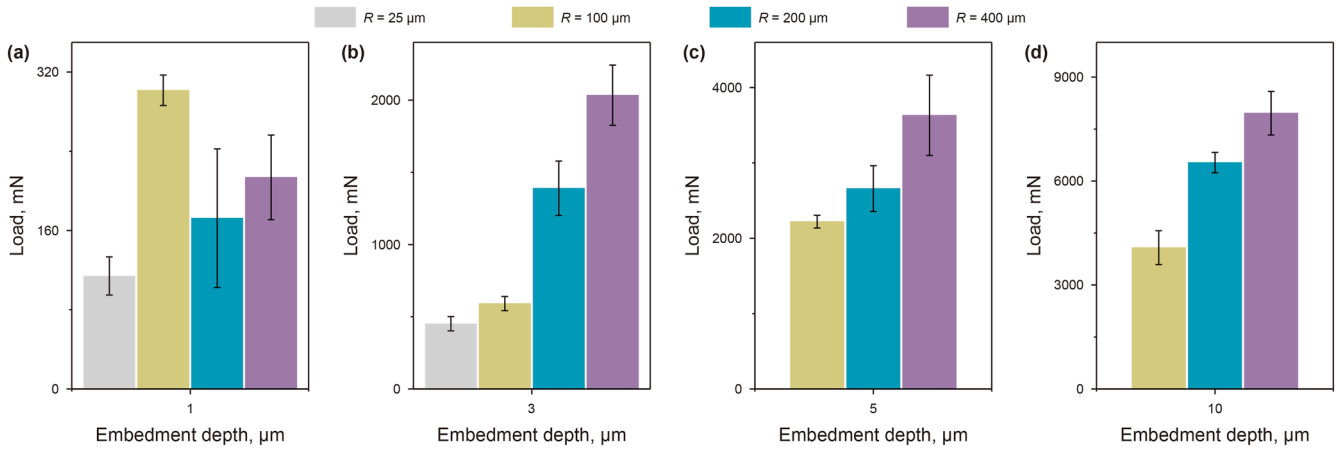


**Fig. 4.** Average load and embedment depth at different radii.

301.6 ± 15.37 mN at 1 μm to 4079.04 ± 488.98 mN at 10 μm, with the relative standard deviation increasing from about 5% to 12%, indicating increasing fluctuation at greater depths. For a 200-μm radius, the load grows markedly from 172.5 ± 70.03 mN at 1 μm to 6531.52 ± 296.49 mN at 10 μm, showing a strong nonlinear increase and enhanced stability with depth. Similarly, the 400 μm radius exhibits a rapid increase in load from 213.63 ± 42.74 mN at 1 μm to 7956.99 ± 629.94 mN at 10 μm, demonstrating the highest bearing capacity among all radii. Overall, larger indenter radii correspond to higher loads at greater embedment depths, while smaller radii and shallow embedment depths exhibit greater variability, reflecting the combined influence of rock heterogeneity and scale effects.

### 3.3. Determination and variation of Young's modulus

Based on the load-displacement curve analysis, the Oliver-Pharr approach can be used to get Young's modulus, which is the primary parameter determining proppant embedment (Oliver and Pharr, 1992). Since the shale surface was penetrated using a spherical indenter, the mechanical parameters are directly applicable to the research of proppant embedment. Fig. 5 displays the average Young's modulus determined by the several indentation tests conducted. Young's modulus is dependent on the indenter radius and embedment depth. A gradual increase in Young's modulus is observed for radii 25 μm and 100 μm when the embedment depth increases from 1 μm to 3 μm. Conversely, a gradual decrease in Young's modulus is observed for radii 200 μm and 400 μm, although their values are still larger than those of radii 25 μm and 100 μm. At an embedment depth of 5 μm, the Young's modulus is nearly the same for different indenter radii, approximately 31 Gpa. Young's modulus steadily lowers as the embedment depth increases from 5 μm to 10 μm, eventually tending close to 25 GPa. Young's modulus variations with depth are consistent when the radii are 25 μm and 100 μm. The mechanical parameter is greatly affected by the radius at a low embedment depth; with the increase of embedment depth, the mechanical parameters measured by different radii are gradually closer. It is evident that the mechanical response varies in different radii at low embedment depths. The mechanical response of various radii progressively approaches as the embedment depth increases.

To assess the repeatability of the indentation measurements, repeated tests were performed under various combinations of indenter radius and embedment depth. The statistical results are summarized in Table 2. The CV values ranged from 3.48% to 18.63%, with most values below 10%, indicating good consistency among repeated measurements.

A slightly higher variability was observed at smaller embedment depths (1–3 μm) and smaller indenter radii (25 μm), which can be attributed to the local heterogeneity of the shale sample. When the heterogeneity within the regional scale is small, the local variation in mineral composition and micro-defects becomes more significant at smaller scales, leading to a noticeable scale

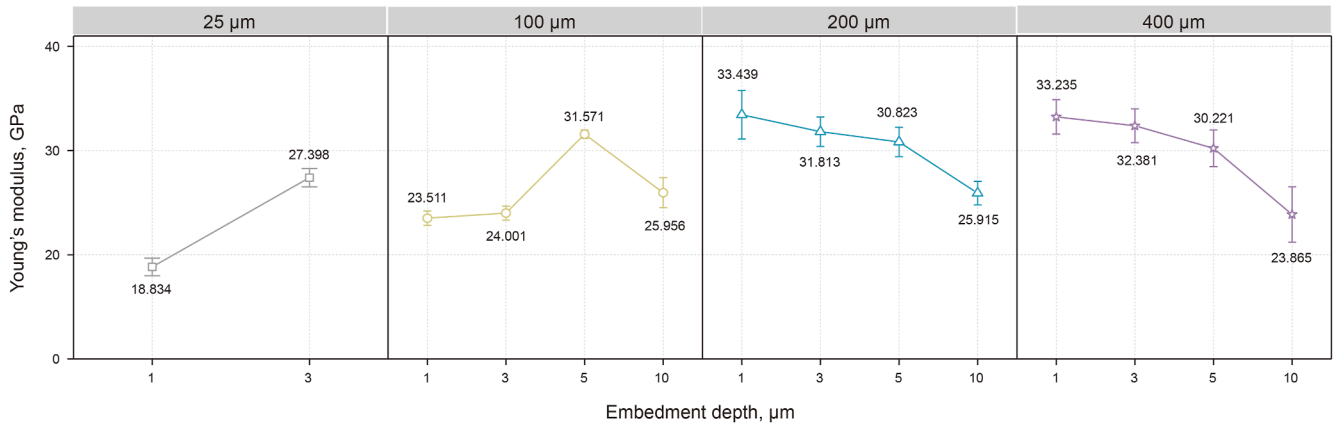


**Fig. 5.** Young's modulus changes at various radii with embedment depth.

**Table 2**
Repeatability statistics for Young's modulus measurements at different indenter radii and embedment depths.

| Indenter radius, μm | Embedment depth, μm | Mean Young's modulus, GPa | SD of Young's modulus, GPa | Difference (max–min) | Lower limit of 95% CI, GPa | Upper limit of 95% CI, GPa | CV of Young's modulus, GPa |
|---|---|---|---|---|---|---|---|
| 25 | 1 | 18.834 | 2.268 | 10.118 | 17.988 | 19.681 | 12.040 |
| | 3 | 27.398 | 2.354 | 10.266 | 26.519 | 28.277 | 8.592 |
| 100 | 1 | 23.511 | 1.843 | 7.775 | 22.823 | 24.199 | 7.837 |
| | 3 | 24.000 | 1.789 | 6.838 | 23.332 | 24.668 | 7.456 |
| | 5 | 31.571 | 1.098 | 4.080 | 31.161 | 31.981 | 3.477 |
| | 10 | 25.955 | 3.862 | 14.056 | 24.513 | 27.397 | 14.878 |
| 200 | 1 | 33.439 | 6.230 | 26.482 | 31.113 | 35.765 | 18.631 |
| | 3 | 31.813 | 3.787 | 15.881 | 30.399 | 33.228 | 11.904 |
| | 5 | 30.823 | 3.784 | 14.161 | 29.410 | 32.236 | 12.276 |
| | 10 | 25.915 | 3.015 | 11.352 | 24.789 | 27.041 | 11.636 |
| 400 | 1 | 33.235 | 4.432 | 15.944 | 31.580 | 34.890 | 13.334 |
| | 3 | 32.381 | 4.344 | 18.181 | 30.759 | 34.003 | 13.416 |
| | 5 | 30.221 | 4.719 | 22.555 | 28.459 | 31.983 | 15.614 |
| | 10 | 23.865 | 4.191 | 12.942 | 21.202 | 26.527 | 17.560 |

effect in the measured response. In contrast, as the embedment depth increases, the probed volume becomes larger and the results tend to average out these local fluctuations, showing improved repeatability. The results confirm that the indentation data exhibit good repeatability.

## 4. Development of an elastoplastic model

Single-particle proppant embedment investigations could provide the foundation for multi-particle response. Proppants are generally thought of as spherical due to their high sphericity. Therefore, ignoring the deformation of the proppant and the stress due to the interaction of adjacent proppant particles, the embedment of single-particle proppant can be abstracted as the penetration behavior of a spherical indenter on the surface of shale. Shale can be considered a nonlinear elastic-plastic material, and during embedment, there are not only elastic stages but also plastic stages. Based on Hertz (1882) contact theory, the elastoplastic embedment model of the spherical indenter penetrating the shale surface is established in the following subsections.

### 4.1. Solution for the elastic model

During the initial contact stage, the contact plane between the proppant and the shale is in the elastic deformation stage. Generally, the Hertz theory is used to describe the elastic contact stage (Johnson, 1985). And the distribution of the contact pressure $p(r)$ can be expressed by Eq. (2):

$$p(r) = p_{\mathrm{m}}(a^2 - r^2)/a \tag{2}$$

where $r$ represents the radial distance from the center of the contact area to any point on the contact surface. When $r = 0$, the maximum contact pressure $p_{\mathrm{m}}$ is expressed as:

$$p_{\mathrm{m}} = \frac{3F}{2\pi a^2} = \left(\frac{6FE^2}{\pi^3 R^2}\right)^{1/3} \tag{3}$$

where $F$ is the indenter load, $a$ is the radius of the circle of contact, $E$ is the elastic modulus, and $R$ is the indenter radius.

The radius of circle of contact $a$ is expressed as:

$$a^3 = \frac{3FR}{4E} \tag{4}$$

The normal compression at any point on the contact surface can be expressed as:

$$\delta(r) = \delta - \frac{r^2}{2R} \tag{5}$$

The distance of mutual approach of distant points in the indenter and specimen is calculated from:

$$\delta = \frac{a^2}{R} \tag{6}$$

Combining Eqs. (4) and (6), the relationship between the indenter load $F$ and embedment depth $\delta$ under the elastic solution is obtained as:

$$F = \frac{4}{3}ER^{1/2}\delta^{3/2} \tag{7}$$

where $\delta = D$ is the embedding depth. Eq. (7) shows that, under the same load, the embedment depth is inversely proportional to the indenter radius.

According to the Hertzian solution, the stress components along the z-axis (normal to the center of the contact surface, $r = 0$), as shown in Fig. 1, can be expressed as follows (Brizmer et al., 2006; Johnson, 1985):

$$\frac{\sigma_r}{p_{\mathrm{m}}} = -(1+\nu)\left[1 - \frac{z}{a}\tan^{-1}\left(\frac{a}{z}\right)\right] + \frac{1}{2}\left(1 + \frac{z^2}{a^2}\right)^{-1} \tag{8}$$

$$\sigma_\theta = \sigma_r \tag{9}$$

$$\frac{\sigma_z}{p_{\mathrm{m}}} = -\left(1 + \frac{z^2}{a^2}\right)^{-1} \tag{10}$$

$$\tau_{rz} = \tau_{r\theta} = \tau_{z\theta} = 0 \tag{11}$$

where $\nu$ is the Poisson's ratio. $\sigma_z$, $\sigma_\theta$, and $\sigma_r$ are the normal stress components in the vertical, circumferential, and radial directions, respectively. $\tau_{rz}$, $\tau_{r\theta}$, and $\tau_{z\theta}$ are the corresponding shear stress components, respectively.

### 4.2. Elastoplastic solution using the Drucker-Prager yield criterion

When the external load on the proppant is large, the shale will yield, and the contact between the proppant and the shale enters the elastoplastic stage. The semi-infinite body is regarded as an elastoplastic material, and it is necessary to introduce the plastic yield criterion. The Drucker–Prager yield criterion is more suitable for reflecting the effect of hydrostatic pressure in stress space during proppant embedment into shale. A previous investigation

found that the Drucker-Prager yield criterion is an appropriate model to examine the inception of plastic behavior for Longmaxi shale (He et al., 2017). The Drucker-Prager yield criterion is expressed as:

$$\alpha I_1 + \sqrt{J_2} = Y \tag{12}$$

where $I_1$ is the first invariant of the stress tensor, $J_2$ is the second invariant of the stress tensor, and $\alpha$ and $Y$ are material yield coefficients.

By setting that $\sigma_1 = \sigma_r$ and $\sigma_3 = \sigma_z$, $I_1$ and $J_2$ are obtained as follows:

$$\begin{cases} I_1 = 2\sigma_r + \sigma_z \\ \sqrt{J_2} = \dfrac{1}{3}(\sigma_r - \sigma_z)^2 \end{cases} \tag{13}$$

By incorporating the stress field during the contact proces (Johnson, 1985), and letting $\xi = \frac{z}{a}$ denote the dimensionless embedment depth, the maximum contact pressure can be expressed as follows:

$$p_m = \frac{Y}{-\left(2\alpha + \frac{1}{\sqrt{3}}\right)(1+\nu)\left[\left(1 - \xi\tan^{-1}(1/\xi)\right] + \frac{\sqrt{3}}{2}\left(1+\xi^2\right)^{-1}} \tag{14}$$

Setting

$$C = \left\{ -\left(2\alpha + \frac{1}{\sqrt{3}}\right)(1+\nu)\left[1 - \xi\tan^{-1}(1/\xi)\right] + \frac{\sqrt{3}}{2}\left(1+\xi^2\right)^{-1} \right\}^{-1}$$

hence,

$$p_m = CY \tag{15}$$

Thornton (1997) believed that the contact pressure was the smallest at the initial displacement, so the partial derivative of the contact pressure was zero at the initial displacement:

$$\left.\frac{\partial p_m}{\partial \xi}\right|_{\xi=\xi_0} = 0 \tag{16}$$

Differentiate the above Eq. (16),

$$\nu = \frac{\sqrt{3}\xi_0}{\left(2\alpha + \frac{1}{\sqrt{3}}\right)\left(\tan^{-1}(1/\xi_0) - \frac{\xi_0}{\xi_0{}^2+1}\right)\left(1+\xi_0{}^2\right)^2} - 1 \tag{17}$$

To further investigate the change of the dimensionless embedment depth $\xi_0$ with respect to variables $\nu$ and $\alpha$, Eq. (17) is expanded in the form of a Taylor series at point $\xi_0 = 0.65$ (He et al., 2023), and the first two terms are retained by Brizmer et al. (2006):

$$\nu = \frac{1.035}{2\alpha + 1/\sqrt{3}} + \frac{1.604}{2\alpha + 1/\sqrt{3}}(\xi - 0.65) - 1 + \cdots \tag{18}$$

From Eq. (18), we obtain the expression for $\xi_0$:

$$\xi_0 = (1.27\alpha + 0.36)\nu + 1.247\alpha + 0.365 \tag{19}$$

The yield displacement $\delta_y$ can be calculated using Eqs. (3), (6) and (15):

$$\delta_y = \left[\frac{\pi}{2}C\frac{Y}{E}\left(1-\nu^2\right)\right]^2 R \tag{20}$$

The yield load $F_y$ can be derived from Eqs. (7) and (20):

$$F_y = \frac{\pi^3}{6}C^3 Y\left(\frac{Y}{E}R\left(1-\nu^2\right)\right) \tag{21}$$

### 4.3. Elastoplastic strengthening model formulation

To analyze the elastoplastic contact problem, Thornton (1997) assumed that the half-space material is an elastic-perfectly plastic body. The contact pressure in the plastic zone of the material after yielding is always constant. Shale always has the characteristic of strain hardening, and the contact pressure is bound to change after yielding. Shale often has strain-hardening properties, and the contact pressure changes continuously after yielding. Based on mechanical tests, it can be observed that shale has a relatively short plastic development stage and strong brittleness before failure, with a stress–strain relationship exhibiting a trend of linear growth. Therefore, a linear strengthening model is used in this paper to describe the elastoplastic embedment of a rigid indenter into shale. Generally, the embedment behavior of a spherical indenter could be equivalently analyzed by applying the methodology used for characterizing the uniaxial tensile/compressive mechanical properties of materials. According to Eqs. (3), (6) and (7), the equivalent stress–equivalent strain relationship for the elastic stage is derived as Eq. (22), in which, $\frac{2a}{\pi R}$ is defined as the equivalent strain:

$$p = \frac{2a}{\pi R}E \tag{22}$$

To establish the relationship between the maximum contact pressure and embedment depth in the elastic stage, by combining Eqs. (3), (6) and (7), Eq. (22) is reformulated as:

$$p_m = \frac{2E}{\pi\sqrt{R}}\delta^{\frac{1}{2}} \tag{23}$$

It can be readily seen that the maximum contact pressure in the elastic range is proportional to the 1/2 power of the compressive displacement. Therefore, it is assumed that the embedment behavior conforms to the elastic-plastic linear strengthening relationship illustrated in Fig. 6.

Combined with the elastoplastic yield displacement of the above Eq. (23), the corresponding constitutive relation can be defined as:

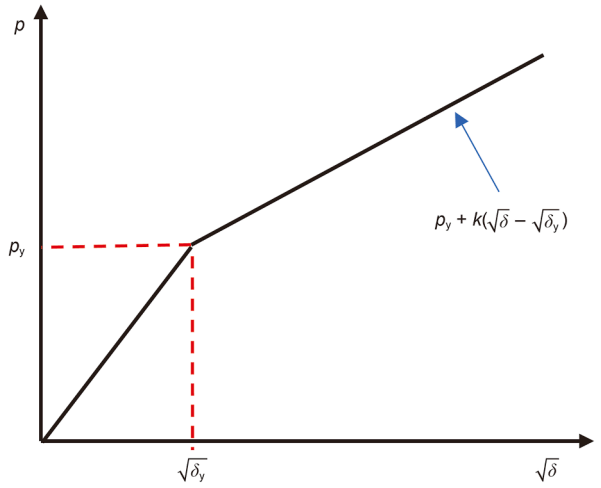


**Fig. 6.** Normal contact pressure-embedment depth model. $p_y$ is the initial yield contact pressure, $\sqrt{\delta_y}$ is the corresponding square root of the initial yield displacement, and $k$ is the post-yield hardening coefficient.

$$p = \begin{cases} \dfrac{2E}{\pi\sqrt{R}}\delta^{\frac{1}{2}}, \sqrt{\delta} \le \sqrt{\delta_y} \\ p_y + k\left(\sqrt{\delta} - \sqrt{\delta_y}\right), \sqrt{\delta} > \sqrt{\delta_y} \end{cases} \tag{24}$$

Eq. (24) shows that when $\sqrt{\delta} > \sqrt{\delta_y}$, both $\delta_y$ and $F_y$ can be computed using Eqs. (20) and (21).

The maximum contact pressure at various embedment depths can be calculated by substituting Young's modulus $E$ into Eq. (23). To derive the evolution of contact pressure at different depths with varied radii, the beginning contact pressure point and maximum contact pressure were linearly connected. Fig. 7 shows the linear growth curves of elastic stages with varied depths at different radii. The maximum contact pressure increases progressively with increasing embedment depth under the same radius. Young's modulus change trend is consistent with the slope change corresponding to different depths. The slope gradually increases as depth grows in Fig. 7(a) and (b), while it gradually lowers as depth increases in Fig. 7(c) and (d).

The linear strengthening (softening) could be expressed by the strengthening coefficient (He et al., 2008). The elastic-plastic constitutive model is an unknown parameter $k$, which can be determined by a macroscopic test. However, the parameter $k$ acquired by a macroscopic test cannot adequately characterize the proppant embedment process since the scale of the indentation test is smaller than that of the macroscopic test. It is evident from the Young's modulus variation trend with depth in Fig. 5 that the embedment depth of the indenter has a significant impact on the mechanical reaction of shale. This demonstrates that the scale effect of shale has a substantial impact on the proppant embedment depth and that the mechanical parameters derived from a single depth are insufficient to describe the proppant embedment process adequately. Therefore, a thorough consideration of the mechanical reaction characteristics at various depths is required to more correctly predict the changes in embedment depth.

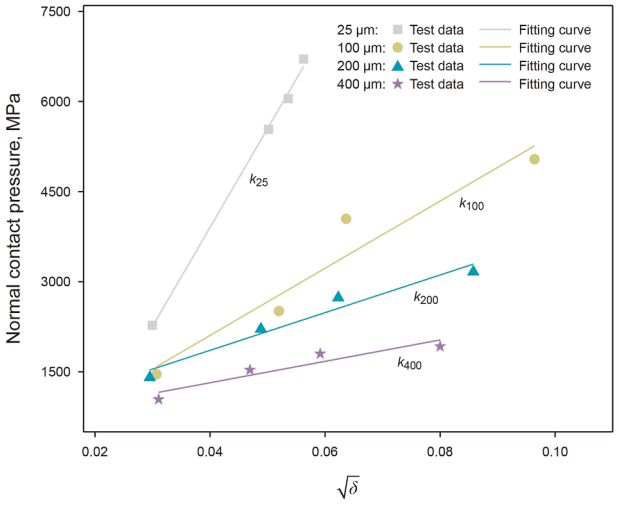


**Fig. 8.** The fitting relationship between normal contact pressure and normal displacement.

This study used a linear fitting method to demonstrate the embedment scale effect of varying radii by analyzing the maximum normal pressure and normal depth at various embedment depths in Fig. 7. The slopes of different inclined lines in Fig. 8 represent the magnitudes of the $k$ values corresponding to different radii. Finally, a semi-empirical relationship was developed to incorporate the effect of shale heterogeneity and to describe the evolution of normal contact pressure with embedment depth for different radii.

To further investigate the size-dependent strengthening behavior in the plastic stage, the relationship between the linear hardening coefficient $k$ and indenter radius $R$ was fitted, as shown in Fig. 9.

The coefficient of determination $R^2$ for the curve fitting is 0.99, indicating a high goodness of fit. The fitting function is as follows:

$$k(R) = 2.08 \times 10^4 + 2.26 \times 10^5 \times \exp(-R/55.1) \tag{25}$$

From the trend of the curve in Fig. 9, there are significant differences in the strengthening characteristics of indenters with different radii, and the strengthening coefficient gradually decreases as the radii increase.

When the contact pressure exceeds the initial yield contact pressure, plastic yielding occurs in the contact region. Combined with Eq. (6), the corresponding relationship for the distribution of normal contact pressure is as follows:

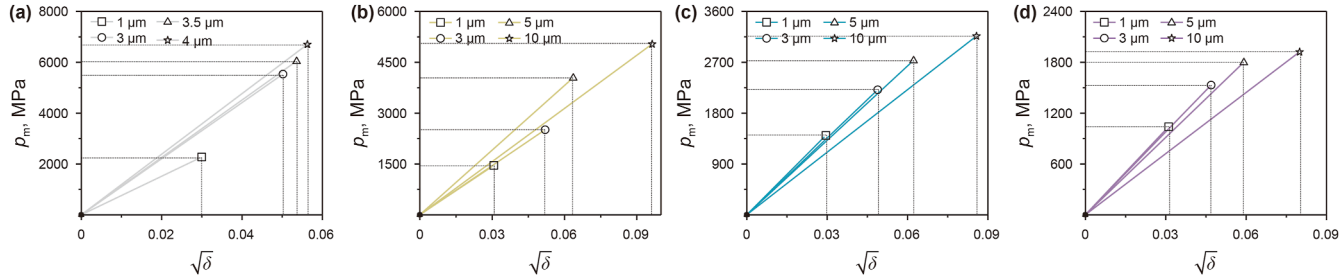


**Fig. 7.** The maximum contact pressure varies with embedment depth at radius of **(a)** 25 μm, **(b)** 100 μm, **(c)** 200 μm, and **(d)** 400 μm, respectively.

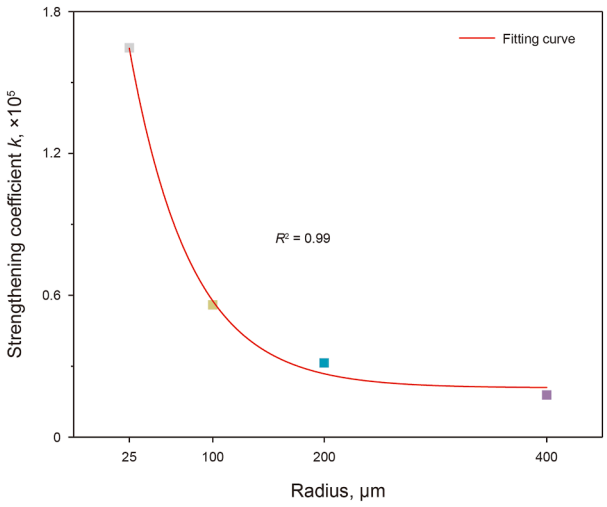


**Fig. 9.** The fitting relationship between the strengthening coefficient and radius.

$$p(r)=\begin{cases} p_y+k(R)\left(\sqrt{\delta-\dfrac{r^2}{2R}}-\sqrt{\delta_y}\right), & 0<r<a_p \\ \dfrac{2E}{\pi R}\left(a^2-r^2\right)^{1/2}, & a_p\le r\le a \end{cases} \tag{26}$$

The contact pressure distribution over the contact area is shown in Fig. 10(a) and (b). In Fig. 10(b), $A_1$ and $A_2$ denote the elastic contact regions, $B_1$ and $B_2$ denote the plastic contact regions. By integrating the normal contact pressure over the contact area, the normal load on the contact surface can be obtained:

$$F=2\pi\int_0^{a_p}\left[p_y+k(R)\left(\sqrt{\delta(r)}-\sqrt{\delta_y}\right]rdr+2\pi\int_{a_p}^{a}\frac{2E}{\pi R}\left(a^2-r^2\right)rdr \tag{27}$$

By integrating Eq. (27), we obtain the normal load-displacement relationship derived based on the elastic-plastic linear strengthening model:

$$F=\pi R(\delta-\delta_y)\left(p_y-k(R)\sqrt{\delta_y}\right)+\frac{4k(R)\pi R}{3}\left[\delta^{\frac{3}{2}}-\left(\frac{\delta+\delta_y}{2}\right)^{\frac{3}{2}}\right]+F_y \tag{28}$$

### 4.4. Comparison and validation of the model with experimental results

To validate the rationality of the theoretical method proposed in this section, the load-displacement curve obtained from indentation tests is used for verification. Based on the research results (He et al., 2023), we take $\nu = 0.2$ and $C = 2.79$. First, the yield parameters are calculated according to Eqs. (20) and (21) respectively, and the two equations are substituted into Eq. (21) to obtain the analytical expression of the theoretical model. Then, the calculation results under different radii are obtained as shown in Fig. 11, which presents a comparison of the normal load-deformation relationships under different radii between the elastic model (Hertz), the elastic-perfectly plastic model (Thornton), the new model (proposed in this paper), and the test data. Fig. 11(c) and (d) show the comparison of the indentation test data at greater depth with the new model. As illustrated in Fig. 11, the load predicted by the proposed model always lies between the Hertz and Thornton models under the same embedment depth. For example, at indentation radii of 25 μm, 100 μm, 200 μm, and 400 μm, the Hertz model overestimates the load relative to the proposed model by 409.1%, 78.9%, 35.3%, and 66.4%, respectively, while the Thornton model underestimates it by 54.5%, 89.7%, 89.8%, and 81.1%. This demonstrates that the new model provides a quantitatively improved prediction, avoiding the significant overestimation of the Hertz model and the strong underestimation of the Thornton model.

## 5. Discussion

Using indenters with four different radii (25 μm, 100 μm, 200 μm, and 400 μm), the elastoplastic embedment behavior of various proppant sizes on a shale surface was examined from an experimental perspective. The findings indicate that variations in embedment behavior might be caused by the multi-scale mechanical characteristics of the shale material. The investigation of several indenters has demonstrated that, depending on the embedment depth, the interaction effect varies between the indenter and the shale. When the embedment depth is low, the embedment behavior of different radii is different. As the embedment depth increases, the radius has a greater influence on the embedment behavior. The load difference of various radii

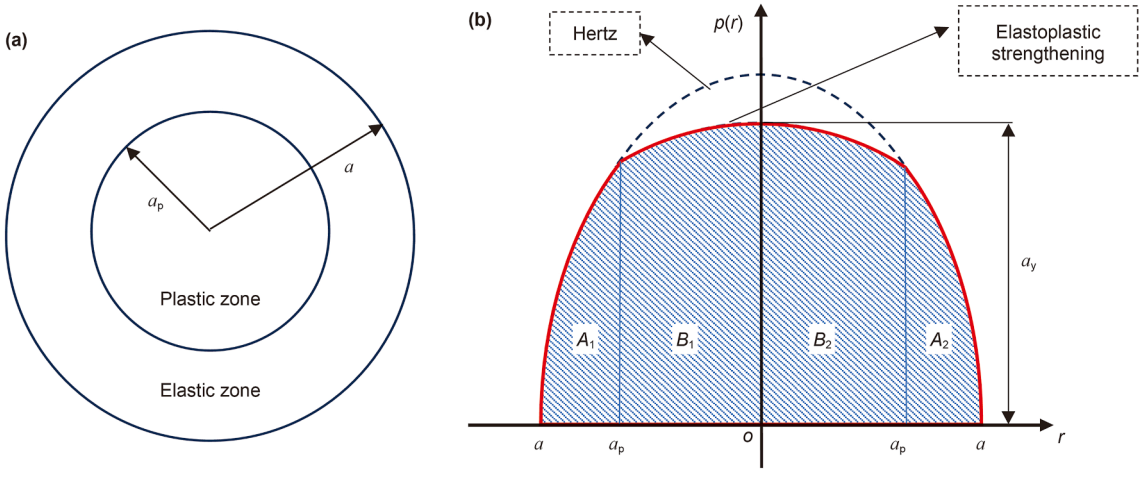


**Fig. 10.** Normal contact pressure distribution on contact surface.

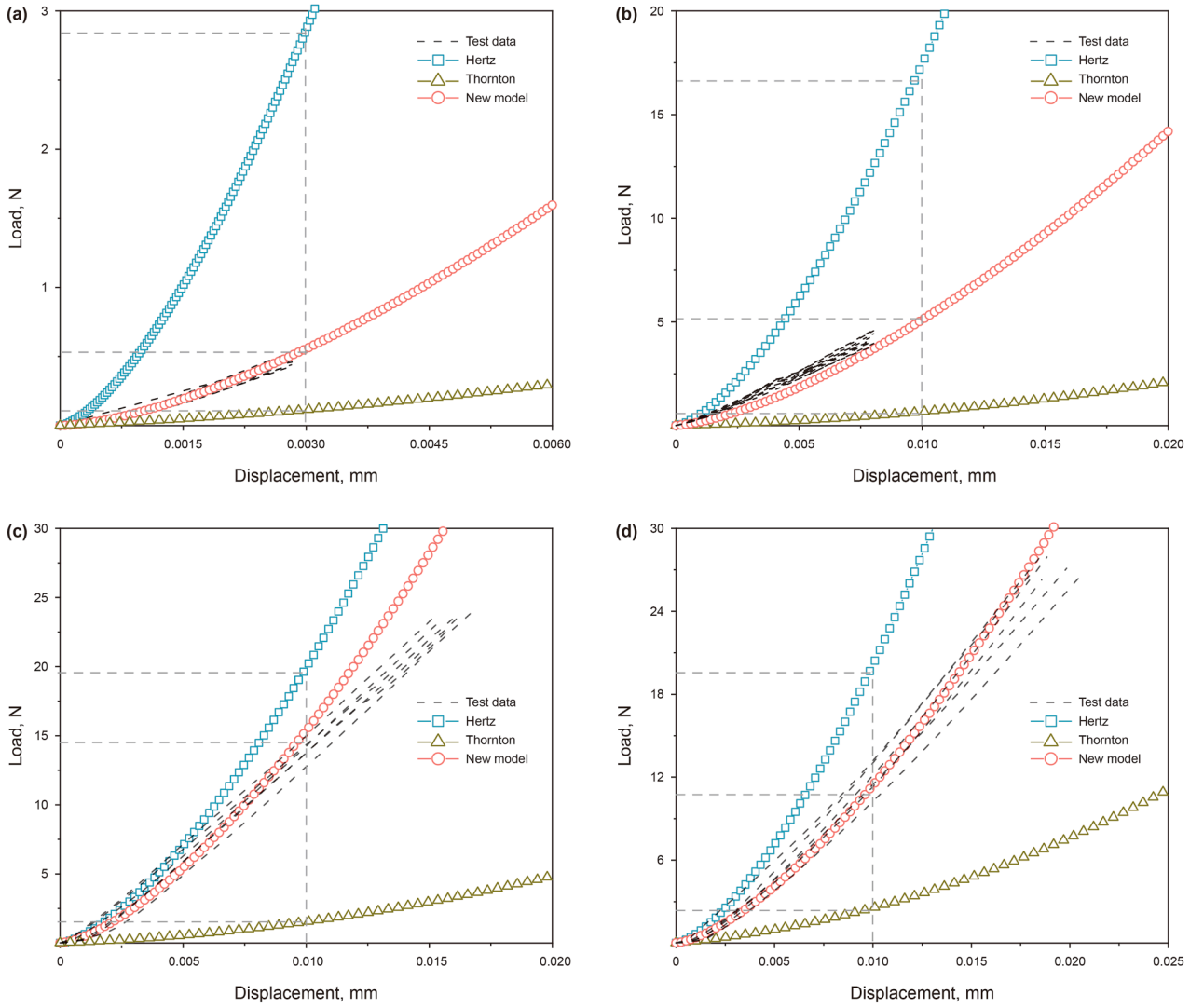


**Fig. 11.** Theoretical models and test data are validated for radii **(a)** 25 μm, **(b)** 100 μm, **(c)** 200 μm, and **(d)** 400 μm, respectively.

gradually emerged as the embedment depth increased, and the mechanical response (Young's modulus) progressively stabilized.

### 5.1. The influence mechanism of size on embedmnt

Firstly, larger-size indenters correspond to higher load at the same embedment depth, indicating the tendency of the larger-size proppants to withstand higher closure pressure (Deng et al., 2014; Zheng et al., 2018). Meanwhile, research indicates that increasing the proportion of sizable proppants can considerably enhance fracture conductivity (Fan et al., 2020; Liu et al., 2021b). Nonetheless, the embedment behavior of proppants tends to weaken when the smaller proppants are placed on the fracture surface since there are more individual particles and contact sites to disperse the applied load (Tan et al., 2017).

Currently, the Berkovich indenter is widely utilized in indentation testing to assess the effect of the mechanical properties of the materials on proppant embedment (Liu et al., 2022a, 2023; Zhi and Elsworth, 2020). Shale has an obvious scale effect. As the indenter penetration depth increases, the elastic parameter eventually becomes stable (Cong et al., 2023; Luo et al., 2020). The mechanical parameters acquired using a spherical indenter are more comparable with the mechanical response of proppant embedment into shale as compared to those obtained with a Berkovich indenter. The spherical indenter has a bigger contact area and a lesser scale effect at the same embedment depth as the Berkovich indenter. In particular, the larger radius can approach the macroscopic mechanical properties at a lower embedment depth.

In this study, Young's modulus of the radii 200 μm and 400 μm are close to each other at various depths, and the value of 100 μm after embedment of 5 μm is close to 200 μm and 400 μm. The embedment difference between varying radii remains distinct even when the scale effect eventually diminishes as embedment depth increases. This may be attributed to the relatively small contact area when the embedment depth is smaller; the mechanical properties of shale at the millimeter scale have a significant impact on the embedment behavior between the indenter and shale. Particularly for indenters with smaller radii, the scale effect of the shale can be significant. However, when embedment depth increases, the larger-scale mechanical characteristics of shale begin to influence embedment behavior. Fig. 7 illustrates how the maximum contact pressure progressively rises with depth. Following yield, there is a significant difference in the plastic strengthening properties of different radii. But as the radius increases, as seen in Fig. 9, the strengthening coefficient progressively falls and eventually levels off, getting closer to the value found in the macro test (Xing et al., 2020).

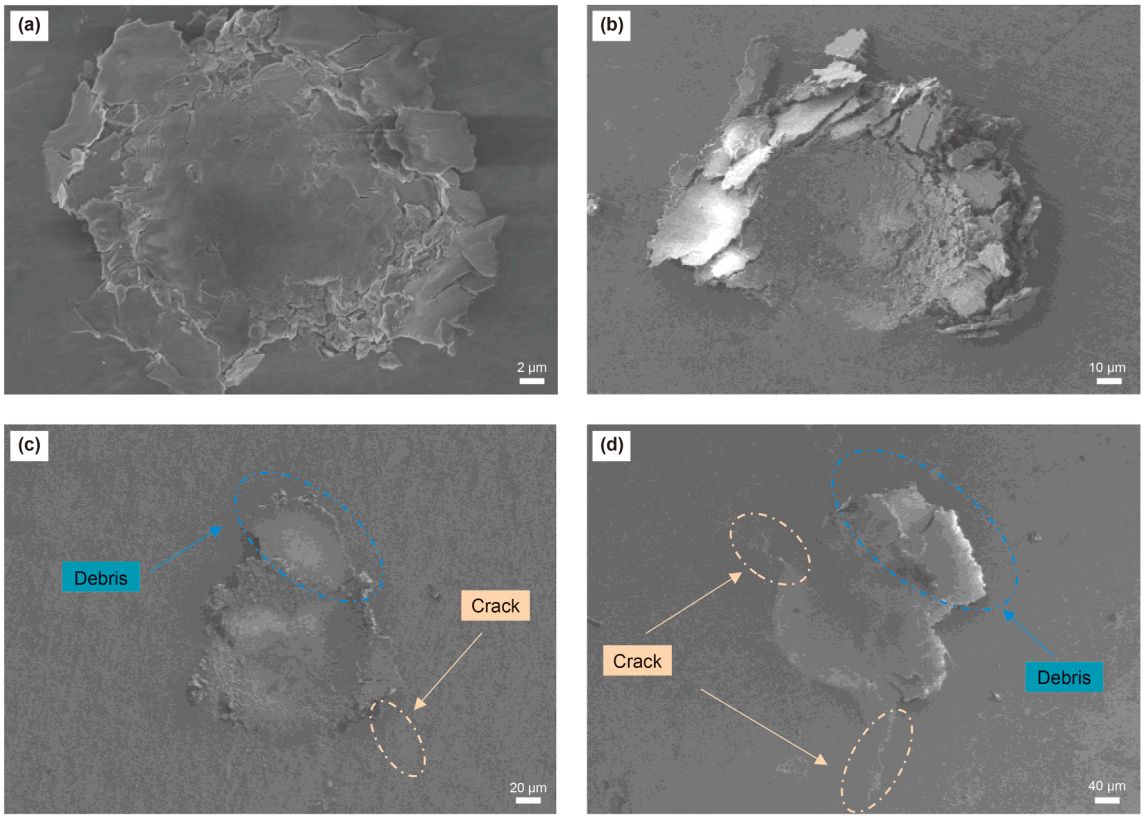


**Fig. 12.** The embedment morphology in radii of **(a)** 25 μm, **(b)** 100 μm, **(c)** 200 μm, and **(d)** 400 μm, respectively.

Fig. 12 shows indentation morphology by SEM with different radii. The observations were conducted under an accelerating voltage of 5 kV, with a working distance of 8 mm, and magnifications ranging from 500× to 2200× . A secondary electron (SE) detector was employed to capture surface morphology. It is apparent that the indentation area continuously rises with an increasing radius. Fig. 12(a) and (b) illustrate that tiny detrital particles predominate at radii of 25 μm and 100 μm, respectively. The amount of tiny particle debris gradually diminishes, and the amount of large particle debris steadily increases as the radius approaches 200 μm and 400 μm. Unexpectedly, at radii of 200 μm and 400 μm, respectively, new developing cracks emerged. The study demonstrates that the proppant embedment will deteriorate the fracture surface of the coal seam (Liu et al., 2021a). Macroscopic fractures are more likely to be observed when the embedment test is conducted with a greater radius of the head and load (Saadati et al., 2020).

### 5.2. Relationship between embedment depth and closure stress

In section 4, the model of indenter load $F$ and embedment depth $\delta$ is obtained. Generally, the relationship between closure stress and embedment depth could be directly applied to the process of oil and gas production. When the proppant is placed in the fracture by hexagonal close packing (Graton and Fraser, 1935), the closure stress $\sigma_c$ and the contact force satisfy the geometric relationship of Eq. (29). Fig. 13 shows the relationship between closure stress and embedment depth. $k$ ($R$ = 25), $k$ ($R$ = 100), $k$ ($R$ = 200), and $k$ ($R$ = 400) represent the strengthening coefficients corresponding to indenters with radii of 25 μm, 100 μm, 200 μm, and 400 μm, respectively.

$$\sigma_c = \frac{1}{2\sqrt{3}} \frac{F}{R^2} \tag{29}$$

Fig. 13 shows that the test results are close to the predicted results of the model. By comparing the Hertz and Thornton embedment models with the new model proposed in this paper, the Hertz and Thornton models illustrate the relationship between embedment depth and radius, but the material considered in these models is all homogeneous, and the material mechanical parameters used in the models are obtained at a single scale. As shown in Fig. 12, the embedment area of the indenter with different radii is inconsistent, and the difference in embedment response will be affected by the multi-scale mechanical properties of shale. To determine the impact of the scale effect on the embedment depth, the comprehensive mechanical response parameter $k$ ($R$) is introduced into the model for comparison.

Fig. 13 shows that under the same closure stress (50 MPa), different strengthening coefficients will lead to significant differences in displacement. Compared with the strengthening coefficient $k$ corresponding to the actual radius, the predicted depth will be higher when a smaller $k$ is selected in the model, while the predicted depth will be lower when a larger $k$ is selected. Fig. 13(a) indicates that the embedment depth is approximately twice as large as the actual embedment depth when the strengthening coefficient $k$ ($R$ = 400) is used, while Fig. 13(d) indicates that the embedment depth is approximately four times smaller than the actual embedment depth when the strengthening coefficient $k$ ($R$ = 25) is used.

In addition, Fig. 13 shows that when the embedment depth is 0.01 mm, the closure stress corresponding to different radii indenter

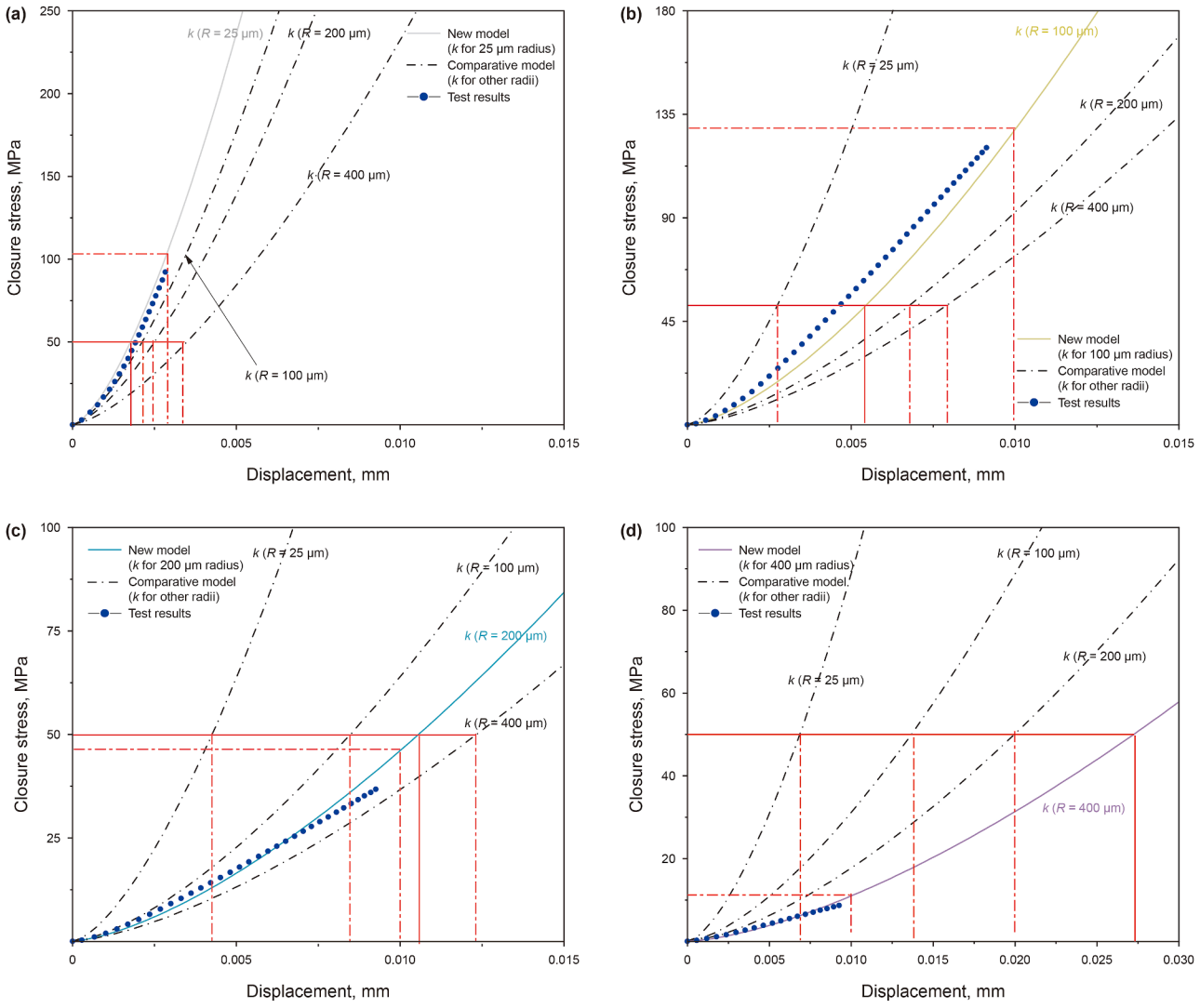


**Fig. 13.** Model prediction results for different strengthening coefficients ($k$) at different radii. **(a)** 25 μm, **(b)** 100 μm, **(c)** 200 μm, **(d)** 400 μm.

is 130 MPa ($R$ = 100 μm), 48 MPa ($R$ = 200 μm), and 12 MPa ($R$ = 400 μm), respectively. A significant inverse connection between the closure stress and the indenter radius at the same embedment depth is found by comparing the change of the closing stress with the indenter radius ($R$ = 100 ~ 400 μm) at various embedment depths (0.001 mm, 0.003 mm, 0.005 mm, and 0.01 mm). The closure stress drops by 92.5% to 91.5% as $R$ rises from 25 μm to 400 μm (i.e., 92.5% at 0.001 mm and 91.5% at 0.01 mm).

In actual reservoir conditions, fracturing fluids often cause degradation of the fracture surfaces, and the embedment depth of proppants tends to increase progressively under long-term closure stress. Therefore, in our future work, we plan to investigate the time-dependent evolution of proppant embedment depth under the influence of fracturing fluid-induced surface degradation. In this study, we idealize the proppant as spherical. However, non-spherical or angular proppants may induce higher stress concentrations at contact edges, promote localized damage, and exhibit reduced contact areas with higher contact stress. Such conditions challenge the applicability of Hertzian theory, requiring advanced contact models or numerical methods for accurate analysis. Future work will also explore the use of non-spherical or angular indenters to simulate more realistic proppant grain shapes and further enhance the representativeness of the experiment test.

## 6. Conclusions

Proppant embedment is a complex process that is affected by many factors, such as fracture surface roughness, closure stress, proppant particle size, and fracturing fluid. To focus on the particle size effect, this study simplified the experimental conditions by polishing the smooth sample surface and investigated the embedment behavior of different radius indenters into the shale surface using the micro-indentation test system. Based on Hertz contact theory and experimental data fitting, a proppant elasto-plastic embedment model was developed. The main findings of this study are summarized as follows:

(1) Different radius indenters exhibit different indentation responses at different embedment depths. At low embedment depths (e.g., 1 μm), the effect of the indenter radius on the load is relatively small, and the variability of the average load is large. As the embedment depth exceeds 3 μm, the effect of the indenter radius on the load gradually increases.

(2) The embedment behavior of the proppant is related to the multi-scale mechanical properties of shale. At low embedment depths, the range of Young's modulus for different indenter radii is large, which is related to the diversity of the small-scale mechanical properties of shale. As the embedment depth increases to 10 μm, the Young's modulus for all indenter radii gradually approaches 25 GPa, indicating that at larger scales, the mechanical properties of shale tend to stabilize, and the influence of the indenter radius diminishes.
(3) The strengthening coefficient steadily decreases as the radius increases, and approaches the macro-scale shale strengthening coefficient in magnitude.
(4) A more accurate embedment depth evolution of different proppant sizes can be acquired by using the strengthening coefficient to describe the plasticity difference of different radii.

## CRediT authorship contribution statement

**Yong-Xin Che:** Writing – original draft, Investigation, Formal analysis. **Ling-Zhi Xie:** Supervision, Project administration, Methodology, Investigation, Conceptualization. **Bo He:** Supervision, Resources, Investigation, Formal analysis. **Yu-Xuan Liu:** Software, Resources, Investigation. **Feng-Xia Li:** Supervision, Resources, Project administration. **Yao Zhang:** Supervision, Software, Formal analysis.

## Declaration of competing interest

Ling-Zhi Xie reports financial support and writing assistance were provided by National Natural Science Foundation of China. The other authors declare that they have no known competing financial interests or personal relationships that could have appeared to influence the work reported in this paper.

## Acknowledgements

This research was funded by the National Natural Science Foundation (No. U23B6004). The authors would like to thank Dr. Yang Liu and Dr. Zhao-Peng Zhang from the Key Laboratory of Deep Earth Science and Engineering (Ministry of Education) at Sichuan University for their useful discussion and experiment assistance in this work. We also would like to thank Dr. Ying-Ming Zhu of Sichuan University for his help in the experimental research.

## References

Ahamed, M.A.A., Perera, M.S.A., Li, D.Y., et al., 2019. Proppant damage mechanisms in coal seam reservoirs during the hydraulic fracturing process: A review. Fuel 253, 615–629. https://doi.org/10.1016/j.fuel.2019.04.166.
Alagoz, E., Wang, H.T., Russell, R.T., et al., 2021. New experimental methods to study proppant embedment in shales. Rock Mech. Rock Eng. 5, 2571–2580. https://doi.org/10.1007/s00603-021-02646-1.
Arshadi, M., Zolfaghari, A., Piri, M., et al., 2017. The effect of deformation on two-phase flow through proppant-packed fractured shale samples: A micro-scale experimental investigation. Adv. Water Resour. 105, 108–131. https://doi.org/10.1016/j.advwatres.2017.04.022.
Bandara, K.M.A.S., Ranjith, P.G., Rathnaweera, T.D., et al., 2021. Crushing and embedment of proppant packs under cyclic loading: An insight to enhanced unconventional oil/gas recovery. Geosci. Front. 12 (6), 100970. https://doi.org/10.1016/j.gsf.2020.02.017.
Bennett, K.C., 2016. The Nanomechanics of Shale: An Experimental and Computational Approach to Constitutive Model Development. Stanford University, Stanford. Ph.D. thesis.
Big-Alabo, A., Harrison, P., Cartmell, M.P., 2015. Contact model for elastoplastic analysis of half-space indentation by a spherical impactor. Comput. Struct. 151, 20–29. https://doi.org/10.1016/j.compstruc.2015.01.005.
Brizmer, V., Kligerman, Y., Etsion, I., 2006. The effect of contact conditions and material properties on the elasticity terminus of a spherical contact. Int. J. Solid Struct. 43 (18–19), 5736–5749. https://doi.org/10.1016/j.ijsolstr.2005.07.034.
Chen, H., Liu, X.L., Zhang, C., et al., 2022. Effects of miscible degree and pore scale on seepage characteristics of unconventional reservoirs fluids due to supercritical $CO_2$ injection. Energy 239, 122287. https://doi.org/10.1016/j.energy.2021.122287.
Chen, M., Zhang, S.C., Liu, M., et al., 2018. Calculation method of proppant embedment depth in hydraulic fracturing. Petrol. Explor. Dev. 45 (1), 159–166. https://doi.org/10.1016/s1876-3804(18)30016-8.
Cong, R.C., Yang, R.Y., Li, G.S., et al., 2023. Geomechanical properties of thinly interbedded rocks based on micro- and macro-scale measurements. Rock Mech. Rock Eng. 56, 5657–5675. https://doi.org/10.1007/s00603-023-03360-w.
Das, D., Mishra, B., Gupta, N., 2021. Understanding the influence of petrographic parameters on strength of differently sized shale specimens using XRD and SEM. Int. J. Min. Sci. Technol. 31 (5), 953–961. https://doi.org/10.1016/j.ijmst.2021.07.004.
Deng, L., Xie, L.Z., He, B., et al., 2024. Anisotropic microscale failure mechanism of shale. Acta Geotech. 19, 7451–7471. https://doi.org/10.1007/s11440-024-02353-5.
Deng, S.C., Li, H.B., Ma, G.W., et al., 2014. Simulation of shale–proppant interaction in hydraulic fracturing by the discrete element method. Int. J. Rock Mech. Min. Sci. 70, 219–228. https://doi.org/10.1016/j.ijrmms.2014.04.011.
Fan, M., Han, Y.H., Gu, M., et al., 2020. Investigation of the conductivity of a proppant mixture using an experiment/simulation-integrated approach. J. Nat. Gas Sci. Eng. 78, 103234. https://doi.org/10.1016/j.jngse.2020.103234.
Fan, M., McClure, J., Han, Y.H., et al., 2019. Using an experiment/simulation-integrated approach to investigate fracture-conductivity evolution and non-darcy flow in a proppant-supported hydraulic fracture. SPE J. 24 (4), 1912–1928. https://doi.org/10.2118/195588-PA.
Fischer-Cripps, A.C., 2007. Introduction to contact mechanics. Mech. Eng. Ser. Appl. Mech. Rev. 55 (3), B51. https://doi.org/10.1115/1.1470678.
Fischer-Cripps, A.C., 2011. Nanoindentation. Mechanical Engineering Series. Springer. https://doi.org/10.1007/978-1-4419-9872-9.
Ghaednia, H., Mifflin, G., Lunia, P., et al., 2020. Strain hardening from elastic-perfectly plastic to perfectly elastic indentation single asperity contact. Front. Mech. Eng. 6, 60. https://doi.org/10.3389/fmech.2020.00060.
Graton, L.C., Fraser, H.J., 1935. Systematic packing of spheres-with particular relation to porosity and permeability. J. Geol. 43 (8), 785–909. https://doi.org/10.1086/624386.
Guo, J.C., Wang, J.D., Liu, Y.X., et al., 2017. Analytical analysis of fracture conductivity for sparse distribution of proppant packs. J. Geophys. Eng. 14 (3), 599–610. https://doi.org/10.1088/1742-2140/aa6215.
He, B., 2021. Study on Non-Linear Embedding Behavior of Proppant of Shale Gas Reservior and the Damage Mechanism to the Fracture Conductivity. Ph.D. thesis. Sichuan university, Chengdu (in Chinese).
He, B., Xie, L.Z., Che, Y.X., et al., 2023. A simplified analytical elastoplastic embedment depth model of proppant based on the Drucker–Prager yield criterion. Rock Mech. Rock Eng. 56 (9), 6207–6217. https://doi.org/10.1007/s00603-023-03394-0.
He, B., Xie, L.Z., Li, F.X., et al., 2017. Anisotropic mechanism and characteristics of deformation and failure of Longmaxi shale. Sci. Sin-Phys Mech As. 47 (11), 114611. https://doi.org/10.1360/SSPMA2016-0053 (in Chinese).
He, S.M., Wu, Y., Li, X.P., 2008. Theoretical model on elastic-plastic granule impact. Eng. Mech. 25, 19–24 (in Chinese).
Hertz, H., 1882. Uber die berührung fester elastischer körper. J. für die Reine Angewandte Math. (Crelle's J.) 92, 156–171. https://doi.org/10.1515/crll.1882.92.156.
Johnson, K.L., 1985. Contact Mechanics. Cambridge University Press, Cambridge. https://doi.org/10.1017/CBO9781139171731.
Katende, A., Allen, C., Rutqvist, J., et al., 2023a. Experimental and numerical investigation of proppant embedment and conductivity reduction within a fracture in the Caney shale, Southern Oklahoma, USA. Fuel 341. https://doi.org/10.1016/j.fuel.2023.127571.
Katende, A., O'Connell, L., Rich, A., et al., 2021a. A comprehensive review of proppant embedment in shale reservoirs: experimentation, modeling and future prospects. J. Nat. Gas Sci. Eng. 95, 104143. https://doi.org/10.1016/j.jngse.2021.104143.
Katende, A., Rutqvist, J., Benge, M., et al., 2021b. Convergence of micro-geochemistry and micro-geomechanics towards understanding proppant shale rock interaction: a Caney shale case study in southern Oklahoma, USA. J. Nat. Gas Sci. Eng. 96, 104296. https://doi.org/10.1016/j.jngse.2021.104296.
Katende, A., Rutqvist, J., Massion, C., et al., 2023b. Experimental flow-through a single fracture with monolayer proppant at reservoir conditions: a case study on Caney shale, Southwest Oklahoma, USA. Energy 273, 127181. https://doi.org/10.1016/j.energy.2023.127181.
Larsson, P.L., Olsson, E., 2016. Elastic-plastic contact between hard metal particles. Key Eng. Mater. 681, 86–99. https://doi.org/10.4028/www.scientific.net/KEM.681.86.
Li, Z.H., Zhao, Q.Q., Teng, Y.T., et al., 2022. Experimental investigation of non-monotonic fracture conductivity evolution in energy georeservoirs. J. Petrol. Sci. Eng. 211, 110103. https://doi.org/10.1016/j.petrol.2022.110103.
Liang, F., Sayed, M., Al-Muntasheri, G.A., et al., 2016. A comprehensive review on proppant technologies. Petroleum 2 (1), 26–39. https://doi.org/10.1016/j.petlm.2015.11.001.
Liu, A., Liu, S.M., Liu, Y.W., et al., 2022a. Characterizing mechanical heterogeneity of coal at nano-to-micro scale using combined nanoindentation and FESEM-EDS. Int. J. Coal Geol. 261, 104081. https://doi.org/10.1016/j.coal.2022.104081.
Liu, W., Zhu, X.S., Li, L., et al., 2021a. Research on the seepage properties of coal with different particle size proppant under cyclic loading. Phys. Fluids 35 (4), 043601. https://doi.org/10.1063/5.0143895.

Liu, X.L., Chen, H., Cheng, W.M., et al., 2025a. Occurrence states and transport behavior of crude oil in different permeability oil reservoirs during depletion development. Geoenergy Sci. Eng. 252, 213944. https://doi.org/10.1016/j.geoen.2025.213944.

Liu, X.L., Chen, H., Li, Y., et al., 2025b. Oil production characteristics and $CO_2$ storage mechanisms of $CO_2$ flooding in ultra-low permeability sandstone oil reservoirs. Petrol. Explor. Dev. 52 (1), 196–207. https://doi.org/10.1016/S1876-3804(25)60014-0.

Liu, Y.W., Liu, S.M., Liu, A., et al., 2022b. Determination of mechanical property evolutions of shales by nanoindentation and high-pressure $CO_2$ and water treatments: a nano-to-micron scale experimental study. Rock Mech. Rock Eng. 55 (12), 7629–7655. https://doi.org/10.1007/s00603-022-03059-4.

Liu, Y.X., Burch, A.C., Bennett, K.C., et al., 2023. Bridging nanoindentation and triaxial creep tests on a shale. Acta Geotech. 18 (12), 6475–6487. https://doi.org/10.1007/s11440-023-02133-7.

Liu, Y.X., Mu, S.X., Guo, J.C., et al., 2021b. Model for fracture conductivity considering particle size distribution in a proppant monolayer. J. Nat. Gas Sci. Eng. 95, 104188. https://doi.org/10.1016/j.jngse.2021.104188.

Liu, Y.X., Wu, L.S., Guo, J.C., et al., 2024. Model for fracture conductivity considering particle size redistribution caused by proppant crushing. Geoenergy Sci. Eng. 240, 213081. https://doi.org/10.1016/j.geoen.2024.213081.

Liu, Y.X., Wu, L.S., Guo, J.C., et al., 2025c. Whole process simulation for efficient proppant placement technology. Geoenergy Sci. Eng. 254, 214045. https://doi.org/10.1016/j.geoen.2025.214045.

Luo, S.M., Lu, Y.H., Wu, Y.K., et al., 2020. Cross-scale characterization of the elasticity of shales: Statistical nanoindentation and data analytics. J. Mech. Phys. Solid. 140, 103945. https://doi.org/10.1016/j.jmps.2020.103945.

Middleton, R.S., Gupta, R., Hyman, J.D., et al., 2017. The shale gas revolution: Barriers, sustainability, and emerging opportunities. Appl. Energy 199, 88–95. https://doi.org/10.1016/j.apenergy.2017.04.034.

Murthy, C.S.N., 2021. Rock Indentation: Experiments and Analyses. CRC Press, Boca Raton. https://doi.org/10.1201/9780429019951.

Oliver, W.C., Pharr, G.M., 1992. An improved technique for determining hardness and elastic modulus using load and displacement sensing indentation experiments. J. Mater. Res. 7 (6), 1564–1583. https://doi.org/10.1557/jmr.1992.1564.

Olsson, E., Larsson, P.L., 2016. A unified model for the contact behaviour between equal and dissimilar elastic–plastic spherical bodies. Int. J. Solid Struct. 81, 23–32. https://doi.org/10.1016/j.ijsolstr.2015.10.004.

Rybacki, E., Meier, T., Dresen, G., 2016. What controls the mechanical properties of shale rocks? – Part II: Brittleness. J. Petrol. Sci. Eng. 144, 39–58. https://doi.org/10.1016/j.petrol.2016.02.022.

Saadati, M., Weddfelt, K., Larsson, P.L., 2020. A spherical indentation study on the mechanical response of selected rocks in the range from very hard to soft with particular interest to drilling application. Rock Mech. Rock Eng. 53 (12), 5809–5821. https://doi.org/10.1007/s00603-020-02242-9.

Shaibu, R., Guo, B.Y., Wortman, P.B., et al., 2022. Stress-sensitivity of fracture conductivity of Tuscaloosa Marine shale cores. J. Petrol. Sci. Eng. 210, 110042. https://doi.org/10.1016/j.petrol.2021.110042.

Tan, Y.L., Pan, Z.J., Liu, J.S., et al., 2017. Experimental study of permeability and its anisotropy for shale fracture supported with proppant. J. Nat. Gas Sci. Eng. 44, 250–264. https://doi.org/10.1016/j.jngse.2017.04.020.

Thornton, 1997. Coefficient of restitution for collinear collisions of elasticperfectly plastic spheres. J. Appl. Mech. 64 (2), 383–386. https://doi.org/10.1115/1.2787319.

Ulm, F.J., Vandamme, M., Bobko, C., et al., 2007. Statistical indentation techniques for hydrated nanocomposites: Concrete, bone, and shale. J. Am. Ceram. Soc. 90 (9), 2677–2692. https://doi.org/10.1111/j.1551-2916.2007.02012.x.

Wang, Y.S., Xu, M., Yang, C., et al., 2020. Effects of elastoplastic strengthening of gravel soil on rockfall impact force and penetration depth. Int. J. Impact Eng. 136, 103411. https://doi.org/10.1016/j.ijimpeng.2019.103411.

Wu, L.S., Liu, Y.X., Guo, J.C., et al., 2025. CFD-DEM simulation of composite plugging using novel sheet fibers in rough fractures. Energy 319, 134895. https://doi.org/10.1016/j.energy.2025.134895.

Xing, Y.K., Zhang, G.Q., Li, S.Y., 2020. Thermoplastic constitutive modeling of shale based on temperature-dependent Drucker-Prager plasticity. Int. J. Rock Mech. Min. Sci. 130, 104305. https://doi.org/10.1016/j.ijrmms.2020.104305.

Zhang, C.P., Liu, S., Ma, Z.Y., et al., 2021. Combined micro-proppant and supercritical carbon dioxide (SC-$CO_2$) fracturing in shale gas reservoirs: A review. Fuel 305, 121431. https://doi.org/10.1016/j.fuel.2021.121431.

Zhang, Y.F., Zhao, Y., Zang, A., et al., 2024. Acoustic emission evolution and hydraulic fracture morphology of changning shale stressed to failure at different injection rates in the laboratory. Rock Mech. Rock Eng. 57 (2), 1287–1308. https://doi.org/10.1007/s00603-023-03586-8.

Zhao, B., Zhang, S., Wang, Q.F., et al., 2015. Loading and unloading of a power-law hardening spherical contact under stick contact condition. Int. J. Mech. Sci. 94–95, 20–26. https://doi.org/10.1016/j.ijmecsci.2015.02.013.

Zheng, W.B., Silva, S.C., Tannant, D.D., 2018. Crushing characteristics of four different proppants and implications for fracture conductivity. J. Nat. Gas Sci. Eng. 53, 125–138. https://doi.org/10.1016/j.jngse.2018.02.028.

Zheng, W.B., Tannant, D.D., Cui, X.J., et al., 2019. Improved discrete element modeling for proppant embedment into rock surfaces. Acta Geotech. 15 (2), 347–364. https://doi.org/10.1007/s11440-019-00819-5.

Zhi, S., Elsworth, D., 2020. Proppant embedment in coal and shale: Impacts of stress hardening and sorption. Int. J. Coal Geol. 227 (3), 103545. https://doi.org/10.1016/j.coal.2020.103545.